Wind and Structures, Vol. 15, No. 3 (2012) 223-245 223
DOI: http://dx.doi.org/10.12989/was.2012.15.3.223

Simulation of multivariate non-Gaussian wind pressure on spherical latticed structures

Nyi Nyi Aung[1], Ye Jihong*[1] and F.J. Masters[2]

[1]*Key Laboratory of Concrete and Prestressed Concrete Structures of Ministry of Education, Southeast University, China*
[2]*Department of Civil and Coastal Engineering, University of Florida, USA*

(Received June 18, 2010, Revised July 1, 2011, Accepted July 20, 2011)

Abstract. Multivariate simulation is necessary for cases where non-Gaussian processes at spatially distributed locations are desired. A simulation algorithm to generate non-Gaussian wind pressure fields is proposed. Gaussian sample fields are generated based on the spectral representation method using wavelet transforms method and then mapped into non-Gaussian sample fields with the aid of a CDF mapping transformation technique. To illustrate the procedure, this approach is applied to experimental results obtained from wind tunnel tests on the domes. A multivariate Gaussian simulation technique is developed and then extended to multivariate non-Gaussian simulation using the CDF mapping technique. It is proposed to develop a new wavelet-based CDF mapping technique for simulation of multivariate non-Gaussian wind pressure process. The efficiency of the proposed methodology for the non-Gaussian nature of pressure fluctuations on separated flow regions of different rise-span ratios of domes is also discussed.

Keywords: domes; wavelet; CDF mapping technique; multivariate; non-Gaussian; stochastic simulation; wind pressure field; wind tunnel experiment

1. Introduction

Simulation of time histories of wind loading is necessary for several wind engineering applications. The objective of this study is to develop a computer simulation technique for the generation of random wind pressure time series (e.g., Seong and Peterka 1997) in order to provide realistic forcing function statistics for fatigue test or for analysis of structural components subjected to fluctuation wind pressures. Gurley and Kareem (1997a) have shown described that highly non-Gaussian localized wind loads are often encountered on structures, particularly in separated flow regions, which may lead to the increased damage on glass panels and higher fatigue effects on building envelope and cladding components. Therefore the development of algorithms to generate sample functions of non-Gaussian stochastic processes and fields (e.g., Huang *et al*. 2000) is critical to address the loading in these regions.

In many cases the non-Gaussian excitations acting on a structure cannot adequately be modeled as a point process at a single location. Large structural systems may be subjected to a number of spatially separated random loads not acting in unison. In order to simulate the response of complex

* Corresponding author, Professor, E-mail: yejihong@seu.edu.cn

nonlinear multiple input systems under extreme conditions, the non-Gaussian loads must be simulated with appropriate correction among components. Li *et al.* (2010) assessed the worst negative wind-induced pressures in the non-Gaussian region of a curved roof by the discretizing and synthesizing of random flow generation technique (DSRFG) which is used to produce a spatially correlated turbulent inflow field for the simulation of wind load. In this paper, the robust simulation techniques in Gurley and Kareem (1998a) are extended to include the simulation of multiple correlated non-Gaussian realization. Signal decomposition using a class of localized basis functions, or wavelets, is a popular new method of nonstationary signal analysis and stochastic simulation. Gurley and Kareem (1997b) have applied wavelet decomposition to the simulation of nonstationary signals through a stochastic manipulation of the decomposition coefficients.

Methods for simulating multi-correlated random signals based on multivariate process with specific cross-spectral density as the sum of sinusoid functions with random phases have been well established and widely used in many engineering applications. Yamazaki and Shinozuka (1988) proposed an iterative method for the generation of sample fields of a multi-dimensional non-Gaussian homogeneous stochastic field with a target power spectral density and marginal distribution function. Deodatis and Micaletti (2002) extended their work to the simulation of multivariate, multi-dimensional non-Gaussian stochastic fields. Grigoriu (1998) also developed a simulation algorithm for generating non-Gaussian stationary translation processes with prescribed marginal distribution and covariance function. A detailed analysis of several non-Gaussian simulation algorithm including performance comparisons is found in Masters and Gurley (2003). These methods are widely accepted for a variety of applications and can reliably produce realizations that match the target power spectral densities (PSDs) and cross-power spectral densities (CPSDs) models of typical domes. A detailed analysis of several non-Gaussian simulation algorithm including performance comparisons is found in Masters and Gurley (2003).

This paper presents a simulation technique to produce multivariate non-Gaussian wind pressure fluctuation using a wavelet transforms approach and a CDF mapping technique. The tool is applicable for both analysis and simulation of structural response and wind pressure data. The simplicity and effectiveness of this methodology is demonstrated using the measured non-Gaussian pressure data from the wind tunnel experiment on the separated regions of the different rise-span ratios of domes by matching with the targets of higher order moment coefficients, wind pressure time series, power spectral densities (PSDs) and cross-power spectral densities (CPSDs).

2. Multivariate non-Gaussian simulation tools

The purpose of this study is to enhance the database of wind tunnel tested dome shapes through existing data sets and application of stochastic simulation algorithms. Considerable work has been done in the simulation of Gaussian processes (Shinozuka and Jan 1972, Borgman 1990, Shinozuka and Deodatis 1991, Girgoriu 1993, Shinozuka and Deodatis 1996) and elements of these methods as well as new techniques have been applied to the simulation of non-Gaussian sample functions (Cai and Lin 1996, Gurley *et al*. 1997, Popescu *et al*. 1998, Masters and Gurley 2003, Grigoriu *et al*. 2007), non-stationary sample functions (Priestly 1967, Vanmarcke and Fenton 1991, Zhang and Deodatis 1996, Li and Kareem 1997), non-Gaussian and non-stationary sample functions (Phoon *et al*. 2002, Sakamoto and Ghanem 2002) and conditional non-Gaussian sample functions (Elishakoff *et al*. 1994, Gurley and Kareem 1998b, Hoshiya *et al*. 1998). The majority of these methods reply on two numerical techniques to infuse prescribed spectral and probabilistic contents into each random signal or field: the spectral representation method (SRM) and the random variable transformation.

2.1 Spectral representation method

This paper addresses the problem of random field simulation by using a wavelet expansion, which is used widely in engineering and science applications (Daubechies 1992). Zeldin and Spanos (1996) introduced the wavelet bases into the simulation of random fields, and reconstructed wavelet coefficients in every scale space based on AR method. Based on Zeldin's method, Kitagawa and Nomura (2003) performed the simulation of one-dimensional random field.

2.1.1. One-dimensional stochastic wind field simulation in wavelet analysis

The orthogonal compactly supported wavelet basis of $L^2(R)$ constructed by Daubechies (1992) wavelets is used in this study. It can be written as

$$\psi_{j,n} = 2^{-j/2}\psi(2^{-j}x - n + 1);\ j, n \in Z \tag{1}$$

where $\psi(x)$ is a wavelet function with support in the segment $[0,2M-1]$; M is an integer parameter and j is scale. The reconstruction algorithm can be expressed as

$$c_k^{j-1} = \langle f_{j-1}, \varphi_{j-1,k}\rangle = \langle \sum_l c_l^j \varphi_{j,l} + \sum d_l^i \psi_{j,l}, \varphi_{j-1,k}\rangle = \sum_l (c_l^j h_{k-2l} + d_l^j g_{k-2l}) \tag{2}$$

where $c_k^j = \int_{-\infty}^{\infty} f(x)\varphi(x)_{j,k}dx$ is a scale coefficient and

$d_k^j = \int_{-\infty}^{\infty} f(x)\psi(x)_{j,k}dx$ is wavelet coefficient.

Using the wavelet decomposition algorithm, the following equations are obtained.

$$r_{k,l}^j = \sum_{n,m=0}^{2M-1} g_n g_m a_{2k+n,2k+m}^{j-1} \tag{3}$$

$$b_{k,l}^j = \sum_{n,m=0}^{2M-1} h_n g_m a_{2k+n,2k+m}^{j-1} \tag{4}$$

$$a_{k,l}^j = \sum_{n,m=0}^{2M-1} h_n h_m a_{2k+n,2k+m}^{j-1} \tag{5}$$

where the procedure is initiated by evaluating firstly the correlation parameters $a_{k,l}^{j-1}$ for the finest scale. Then, substituting $a_{k,l}^{j-1}$ into Eqs. (3) and (4), $r_{k,l}^j$, $b_{k,l}^j$ and $a_{k,l}^{j-1}$ can be determined. Using the ARMA(p,q) model, the wavelet coefficient, $\boldsymbol{d}^j$, can be generated from

$$\boldsymbol{d}_k^l = \sum_{i=1}^{p} \boldsymbol{\alpha}_i \boldsymbol{c}_{k-1}^j + \sum_{i=0}^{q} \boldsymbol{\beta}_i \boldsymbol{u}_{k-1} \tag{6}$$

where $\boldsymbol{u}_k$ are the uncorrelated zero mean, unit variance random variables that are statistically independent of c_k^j.

A higher order AR model (AR(p)) is appropriately equivalent to ARMA(p,q),($p1 >> p$) , so it can be used to determine ARMA model parameter. AR($p1$) model can be expressed as the following form.

$$d_k^j = [\alpha_1 \ldots \alpha_{p1}][c_{k-1}^j \ldots c_{k-p1}^j]^T + \beta_0 u_k \tag{7}$$

Using the solutions of Eqs. (3), (4), (5) and (7), $\boldsymbol{\alpha}$, $\boldsymbol{\beta}$ can be calculated. $\boldsymbol{\alpha}$, $\boldsymbol{\beta}$ are required to solve once for each scale . Then, they can be substituted into Eq. (6) to compute $\boldsymbol{d}_k^j$.

2.1.2 Simulation of multiple wind time histories

A large class of problems in stochastic analysis requires the generation of correlated multiple random processes. Spinelli *et al*. (1987) suggested the simulation procedure that minimizes computational time and storage. In order to obtain the specified spectral densities for the processes $u(t)$, the individual spectra $S_u^{ii}(n)$ are divided into two constitutive elements, $S_v^{ii}(n)$ and $S_\varepsilon^{ii}(n)$.

$$S_u^{ii}(n) = S_v^{ii}(n) + S_\varepsilon^{ii}(n) \tag{8}$$

where $S_v^{ii}(n) = S_v(n)$ is the spectrum of the processes $v^j(t)$, chosen as the common area of individual spectra $S_\varepsilon^{ii}(n)$; and $S_\varepsilon^{ii}(n)$ is the spectrum of the process $\varepsilon^i(t)$.(Fig. 1)

A family of correlated random processes

$$u(t) = \boldsymbol{L}v(t) + \varepsilon(t) \tag{9}$$

where $\boldsymbol{L}$ is a lower triangular matrix to be determined.

It can be shown that, in order to impose the specified cross-correlation matrix at zero time lag,

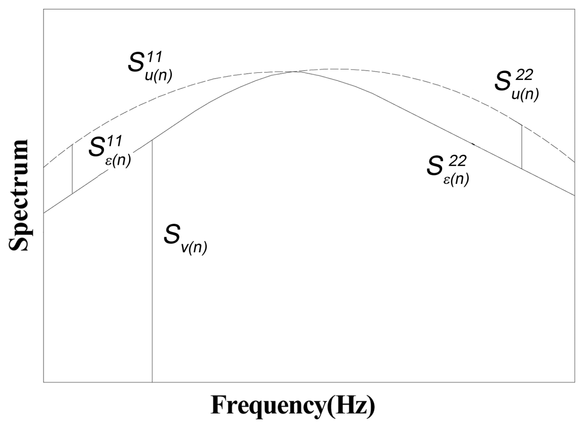

Fig. 1 Spectra $S_u^{ii}(n)$, $S_v(n)$ and $S_\varepsilon^{ii}(n)$

$\bar{\boldsymbol{R}}_u(0)$, the lower triangular matrix $\boldsymbol{L}$ in Eq. (9) must be satisfy the relationship.

$$\bar{\boldsymbol{R}}_u(0) = \boldsymbol{L}\boldsymbol{L}^T \tag{10}$$

where

$$\overline{R_u^{ij}}(0) = R_u^{ij}(0) - \delta^{ij}(\sigma_\varepsilon^{ii})^2 \tag{11}$$

This is related to with the cospectrum by the Wiener-Khinchin equation (Bendat and Perisol 1986). where

$$R(\tau) = \int_{-\infty}^{\infty} S(n)\cos(2\pi n\tau)dn \tag{12}$$

is determined; then

$$R_u^{ij}(0) = \int_0^{\infty} S_u^{ij}(n)dn \tag{13}$$

but

$$(\sigma_\varepsilon^{ii})^2 = \int_0^{\infty} S_\varepsilon^{ii}(n)dn \tag{14}$$

$\boldsymbol{L}$ in Eq.(10) can be calculated by a Choleski factorization of $\bar{\boldsymbol{R}}_u(0)$. After $\boldsymbol{L}$ is determined, $v(t)$, $\varepsilon(t)$ and $\boldsymbol{L}$ can be substituted into Eq.(9). Thus the series of wind pressure time histories with spatial correlation can be obtained.

2.1.3 Algorithm of wavelet analysis

Summarizing the preceding discussion, the proposed algorithm for synthesizing random fields specified by the auto-correlation function can be formulated as follows:

(1) Select the appropriate wavelet basis. Note that these wavelets are differentiable functions and generated field can be readily used in applications necessitating differentiation of the generated field samples.

(2) Find the correlation of the wavelet and scale coefficients using Eqs.(3)-(5).

(3) Synthesize a sample of the random process for a relatively coarse scale j by simulating a small-dimensional vector, c^j.

(4) Generate the vector $\boldsymbol{d}^j$ by using Eq. (6).

(5) Based on the realizations of c^j and d^j, synthesize a sample of the random process on the next (j–1) scale by using Eq. (2).

(6) If the ratio of the wavelet coefficients to the variance of the scale coefficients is not adequately small, proceed to a refined scale and return to Step (4).

(7) Extend multivariate Gaussian simulation from univariate Gaussian simulation using the approach detailed in section 2.1.2.

2.2 Random variable transformation

Three typical forms of the random variable transformations are given below

(a) Analytical Filter

When available, a deterministic equation is often the most efficient approach to altering the probability content a stochastic sample function. The modified Hermite polynomial is one such transformation, and its details are explained further in the Hermite-based spectral correction section (e.g., Gurley *et al*. 1997).

(b) Empirical or Analysis Gaussian to Non-Gaussian Mapping

Grigoriu *et al*. (1984) used the following relationship to map a Gaussian signal $u(t)$ into a prescribed non-Gaussian signal $x(t)$ through their respective cumulative distribution (CDF) functions: the prescribed non-Gaussian cumulative distribution function F_x and the Gaussian cumulative distribution function $\Phi[\ ]$.

$$x(t) = F_X^{-1}(\Phi[u(t)]) \tag{15}$$

This translation can either take the form of an analytical relation, or an empirical mapping scheme.

(c) Empirical Non-Gaussian Mapping

Deodatis and Micaletti (2002) expanded the Gaussian to non-Gaussian mapping concept by generalizing to an empirically based non-Gaussian to non-Gaussian CDF mapping. Masters and Gurley (2003) developed a spectral correction algorithm based on CDF mapping technique by modifying the technique of Deodatis and Micaletti (2002).

$$x(t) = F_X^{-1}(F_{\hat{X}}[\hat{x}(t)]) \tag{16}$$

where the arbitrary non-Gaussian sample function $\hat{x}$ is mapped through its CDF $F_{\hat{x}}$ into the cumulative distribution F_X to create a sample function $\boldsymbol{x}$, non-Gaussian.

2.2.1. CDF map-based spectral correction

Using a general non-Gaussian CDF mapping technique (Masters and Gurley 2003), the multivariate Gaussian simulation process can be transformed to generate multivariate non-Gaussian simulation. This algorithm is easily programmed and is very robust and reliable in its convergence to the desired PSD. This convergence is demonstrated to be discussed in coming up section. Fig. 2 illustrates the procedures of this simulation technique. There are four portions in CDF map-based spectral correction algorithm.

(1) Establish targets for the power spectral density (PSD), S_{xx}^T and coherence function, γ_{ij}^2.

(2) Create a univariate Gaussian sample function using the spectral representation method (SRM) such as wavelet transform method.

(3) Extend multivariate Gaussian simulation from univariate Gaussian simulation using the approach detailed in section 2.1.2

(4) Begin the iterative procedure

(a) Correct the probability to the target using non-Gaussian CDF mapping. This leaves the correct probability but distorted spectral contents.

(b) In the frequency domain, the phase of the signal is maintained and the Fourier amplitude to match S_{xx}^T is replaced. The signal now has the correct spectral content but distorted probability.

(c) Qualify the probability distortion by measuring error in skewness and kurtosis with respect to

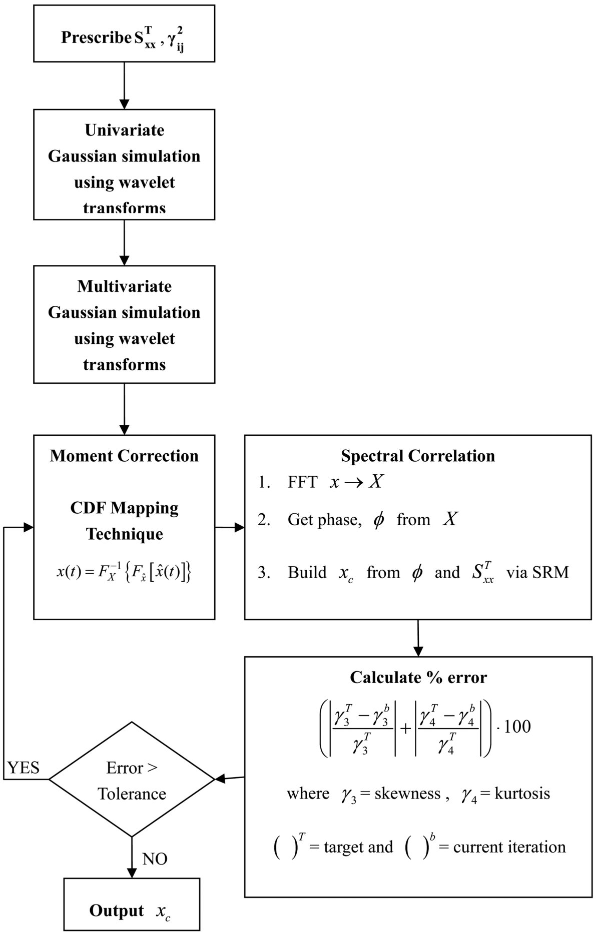

Fig. 2 CDF map-based spectral correction using wavelet transforms

the target values established from the first CDF mapping iteration.
(d) If the error is less than a user-determined tolerance, the simulation is complete.
(e) Otherwise, repeat steps (a)-(c).

2.2.2. Concept of CDF mapping technique

The CDF mapping of algorithm requires an additional consideration for second and higher iterations. After frequency domain spectral correction, the CDF of the sample function, $F_{\hat{X}}$, is a function of the specific corrections to the Fourier coefficients and changes with each iteration. Masters and Gurley (2003) discuss that a signal of infinite length has an empirically determined CDF bounded by zero and unity. However, the empirical CDF of a finite length signal is bounded by [1/(M+1)L M/(M+1)], where M equals the number of points in the signal. Application of Eq. (16) maps this empirical CDF $F_{\hat{X}}$ into an analytical CDF. The cumulative distribution range of the sample function is adjusted from [1/(M+1) ··· M/(M+1)] to ($\varepsilon_1 L$, ε_2), where ε_1 approaches zero and ε_2 approaches to unity. After the initial Gaussian process is generated, the random minimum and maximum values of the process are compared to normal cumulative distributions to determine the minimum and maximum F-values. These minimum and maximum probabilities are set as the limits (ε_1L, ε_2) for the empirical CDFs ($F_{\hat{X}}$) that are then mapped to the desired CDF.

2.2.3. Validation and limitations of the simulation algorithm

This section discusses the efficiency, limitations and accuracy of the multivariate stochastic simulation algorithm developed in this study. In this paper, it is shown that the algorithm simulates as many as four pressure taps of varying correlation on the angles of direction of domes successfully. The target coherence function in this simulation depends on the angles of direction of dome, frequency interest and separation distances.

During the development of the simulation software, the several exponentially decaying spectral models (adapted from wind PSDs) were tested to improve the accuracy and robustness of the algorithm. It is depended on the windward and leeward sides of domes because the spectra in these sides have same characteristics. Due to the same target of spectra in each side, the length of simulation time is shorter than the time consumption of the different characteristics of spectra.

Lastly, it should be noted that the univariate Gaussian simulation can then be transformed into the simulation of multivariate non-Gaussian wind pressure using the help of a wavelet-based CDF mapping technique with the aid of iteration. Thus, the simulated cross-power spectral densities can be obtained to match with their targets on each direction. It affects the temporal correlation structure but reduces the number of non-positive definite matrices in the Cholesky decomposition. Given the close proximity of the pressure taps, this simplification are determined to have a negligible effect on simulation results. Masters *et al*. (2004, 2010) found that the spectral analysis reveals that imaginary components make up less than 2% of the magnitude of the CPSD ordinates (the phase < ~0.02 radians).

2.2.4. Accuracy of the simulation algorithm

Previous studies have demonstrated the accuracy of the simulation method for generating realizations that match the input targets (cf. Deodatis and Micaletti 2002, Grigoriu *et al*. 1998, Masters and Gurley 2003). Simulations were performed for each angle of direction including wind direction and compared against PSD target models to validate the accuracy of the algorithm.

In this simulation algorithm, the CDF mapping procedure is applied to the individual taps as the last step before dilation and translation to install the proper first and second moments. The accuracy of this mapping procedure has been shown to be highly accurate, and thus the probability descriptors for the individual taps will match the targets without fail (Masters and Gurley 2003). Therefore, an explicit comparison of target and simulated PDFs is not provided. However, accuracy is confirmed for this study. A quantitative comparison of higher order moments is provided in the results section when the simulation algorithms are generated.

3. Cases studies

3.1 Wind tunnel datasets on the domes

The pressure data used in this study was collected from wind tunnel at the Wind Engineering Research Center of Hunan University in China. Two models is 1/200 models were used. The first dome model is made of FRP and has a rise-span ratio of 1:2 (Fig. 3). The second is made of

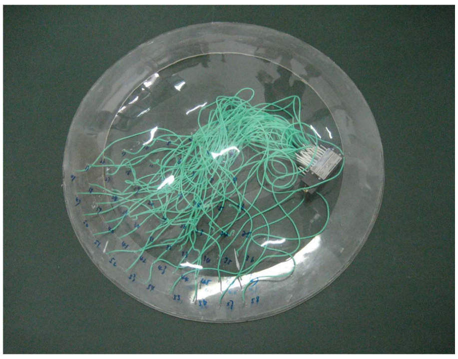

Fig. 3 Testing points on dome model

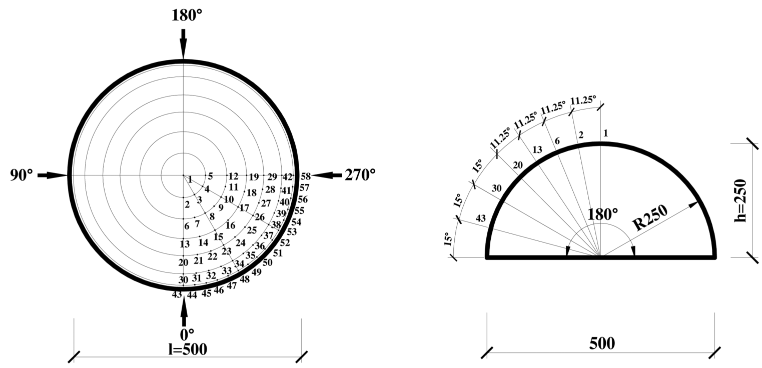

Fig. 4 Wind tunnel testing points on dome (h:l =1:2)

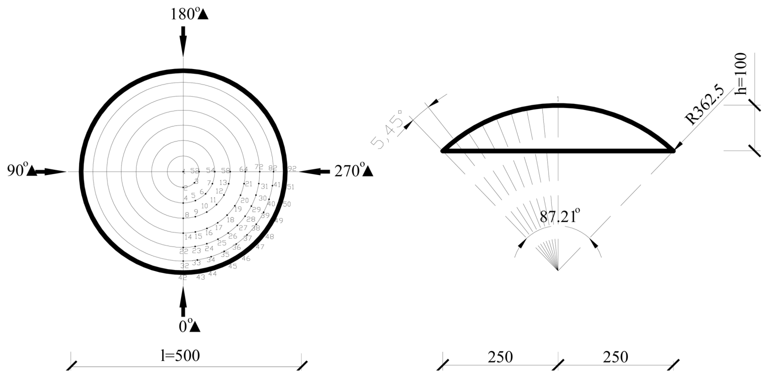

Fig. 5 Wind tunnel testing points on dome (h:l =1:5)

organic glass and has a rise-span ratio of 1:5. Data was collected at 325 Hz using a Scanivalve system. In total data was collected from 24 incident wind angles, with a 15° separation. Data was recorded for nominally 20 seconds (6600 data points). The pressure tap grid is shown in Figs. 4 and 5.

3.2 Regions of Gaussian and non-Gaussian regions on domes

Based on skweness and kurtosis values, the measured time histories have subsequently been

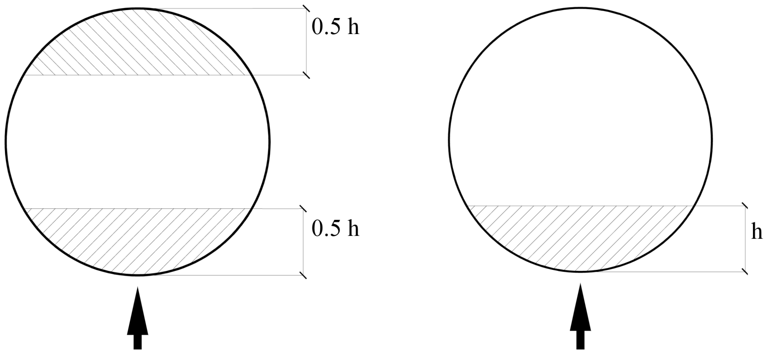

(a) Dome (h:l=1:2) (b) Dome (h:l=1:5)

Fig. 6 Gaussian and non-Gaussian zones on domes

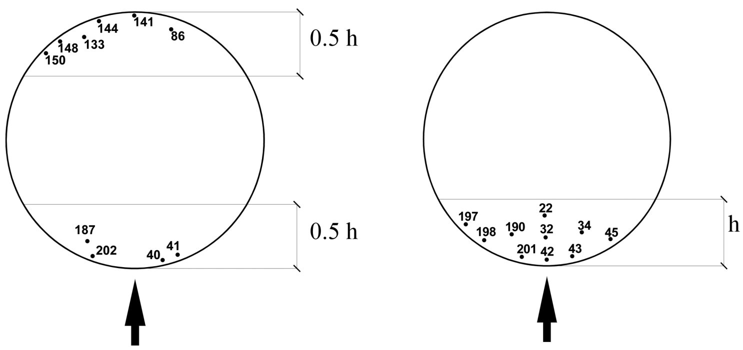

(a) Non-Gaussian Region (h:l=1:2) (b) Non-Gaussian Region (h:l =1:5)

Fig. 7 Locations of non-Gaussian points on domes

classified into Gaussian and non-Gaussian regions. Theoretically, the skewness and kurtosis are 0 and 3 for Gaussian region. In the practical application of wind engineering, there is no a unified criterion to define Gaussian and non-Gaussian feature of wind pressure. Concerning this issue, Sun *et al*. (2007) brought forward two principles for determining dividing standards: (1) the relations between skewness and kurtosis satisfy a certain changing trend; (2) exceeding probabilities for skewness and kurtosis are nearly the same. According to the above two principles, values of skewness and kurtosis of domes are calculated. Thus, in this study, the measured pressure taps with absolute values of skewness and kurtosis greater than 0.5 and 3.5 are classified into non-Gaussian region respectively. Fig. 6 shows the distribution of Gaussian and non-Gaussian regions on domes, in which the shaded parts represent the non-Gaussian regions and h is the dome height. The non-Gaussian pressure taps on different types of domes were collected on zero wind direction (Fig. 7).

3.3 Power spectral density (PSD) models and coherence model

The spectral representation method (SRM) requires target PSDs to generate Gaussian signals. Based on the similarities found in spectra for various zones, a suitable analytical model was adapted to produce a universal pressure spectra model for simulation. Within this context, several well-known curve-fitting techniques have been employed to extract a suitable target for spectra. Using a least-square fitting method, the two-term exponential model, $y = a \exp(bx) + c \exp(dx)$, gives a better statistical fit than other models. A detailed analysis procedures of fitting method with the help

Table 1 Estimation of parameters for target power spectrum density

Dome types	Zone	a_1	a_2	c_1	c_2
$h{:}l$ = 1 : 2	windward	0.0027	0.000068	0.2661	0.1987
	leeward	0.0015	0.000046	0.2321	0.2085
$h{:}l$ = 1 : 5	windward	0.0005	0.000023	0.2200	0.2353

of MATLAB can be found in Kumar *et al*. (1997) and, Kumar and Stathopoulos (1998). Both two types of domes are assigned the same non-Gaussian target spectral density function S_{xx}^T given by

$$S_{xx}^T(f) = a_1 exp(-c_1 f) + a_2 \exp(-c_2 f) \tag{17}$$

where $S_{xx}^T(f)$ is the target spectral density function, f is the interest of frequency, a_1 and a_2 are the position constants and c_1 and c_2 are the shape of constants.

Moreover, frequency of interest, separation distances and angle of direction might be emphasized and that allows for reduction in coherence with increase separation and change of angle of direction. This exponential coherence model (Nyi and Ye 2010) can be expressed as

$$\gamma_{ij}^2(f, L_{ij}, \theta) = \left\{ aH\cos\left(\frac{\theta}{2}\right)\exp(bf)^{\frac{1}{4}} + cH cos\left(\frac{\theta}{2}\right)\exp(bf)^{\frac{1}{4}} \right\}^2 \tag{18}$$

where H is denoted by $\frac{(D-L_{ij})}{D}$ and L_{ij} is $\sqrt{(x_j-x_i)^2+(y_j-y_i)^2+(z_j-z_i)^2}$. Here, L_{ij} is separation distance of two testing points at points i and j; (x_i, y_i, z_i) and (x_j, y_j, z_j) are coordinates at points i and j; f is frequency of interest; θ is angle of direction from wind direction; and D is span of dome. The overall least-squares fit parameters a, b, c and d for exponential model for coherence function were 0.8656, -0.1037, 0.1852 and -0.0152, respectively.

3.4 Measurement of Error

Quantifying probabilistic and spectral deviation in the simulation from their respective defined targets depends upon the application of the simulation. It is described in Eq. (19).

$$3^{rd} \text{ and } 4^{th} \text{ Central Moment Error} = \left|\frac{\gamma_3^T - \gamma_3^b}{\gamma_3^T}\right| + \left|\frac{\gamma_4^T - \gamma_4^b}{\gamma_4^T}\right| \tag{19}$$

where γ_3 = skewness , γ_4 = kurtosis and $(\ )^T$ = target and $(\ )^b$ = current iteration

If the error is within the specified tolerance, the algorithm stops and non-Gaussian process is output with the target spectrum S_{xx}^T. If the error is not within the specified tolerance, next iteration is begun. Here, the kurtosis value is a more robust characteristic since it summarizes the effect of all excessive peaks, which make the non-Gaussian. In many cases (e.g., Steinwolf *et al*. 2006, Steinwolf and Stepten 2006), the high skewness of the field data can be negligible, and it can be emphasized in terms of kurtosis only to get target values, which now will become a single target for the CDF mapping transformation.

4. Results of multivariate non-Gaussian simulation

The targets of power spectral density models and coherence model are required to develop the simulation of multivariate non-Gaussian wind pressure fields on the domed structures. The target coherence model in this simulation depends on the angles of direction of the domes, frequency interest and separation distances. Thus we collect the study taps on the angles of direction of the domes shown in Fig. 8.

4.1 Targets and simulations of skewness and kurtosis coefficient

Cases (1-2) are considered for both windward and leeward sides of different rise-span ratios of domes using two pressure taps. Cases (3-4) consider the windward side of the dome ($h:l$=1:5) using three and four pressure taps respectively. All pressure taps are shown in Fig. 8. These cases show the sum of the percent difference between the target and simulated values and the percent difference from target kurtosis in Table 2.

From Cases (1-4), one common feature of the target signals is that they are positively skewed on

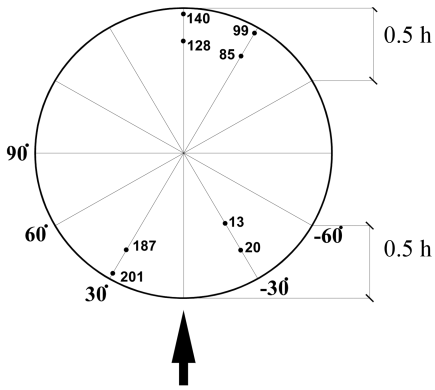

(a) Study taps on dome ($h:l$=1:2)

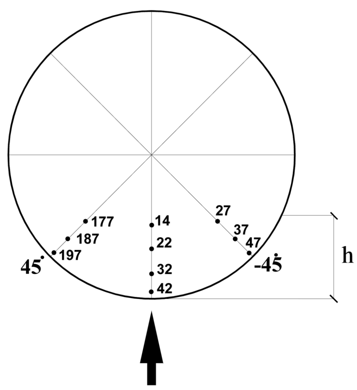

(b) Study taps on dome ($h:l$=1:5)

Fig. 8 Pressure taps location on the dome models

Table 2 Resultant errors in the skewness and kurtosis values of simulation

Case (1) Two pressure taps non-Gaussian simulation of dome ($h:l$=1:2) (windward and leeward)

Point*	Skewness		Kurtosis		Sum of % diff. from target	% diff. from kurtosis target
	Target	Simulated	Target	Simulated		
13	0.4375	0.4823	4.0594	4.0823	10.8041%	0.5641%
20	0.4086	0.4648	4.0510	4.0548	13.8481%	0.0938%
85	-0.5047	-0.4026	3.5791	3.7171	24.0856%	3.8557%
99	-0.5282	-0.4179	4.0284	4.1515	23.9381%	3.0558%
128	-2.0244	-2.4128	19.4050	19.9220	21.8502%	2.6643%
140	-0.8156	-0.6359	5.1505	5.2491	23.9472%	1.9144%
187	0.5400	0.4597	3.6515	3.6672	15.3003%	0.4300%
201	0.4618	0.5607	3.6383	3.6323	21.5811%	0.1649%

Case (2) Two pressure taps non-Gaussian simulation of dome (*h:l*=1:5) (windward)

Point*	Skewness		Kurtosis		Sum of % diff. from target	% diff. from kurtosis target
	Target	Simulated	Target	Simulated		
22	0.7254	0.7418	4.6915	4.6822	2.4591%	0.1982%
32	0.6023	0.5215	3.8021	3.8004	13.4600%	0.0447%
37	0.5311	0.6708	3.8384	3.8697	27.1193%	0.8154%
42	0.6542	0.5085	3.7300	3.7392	22.5181%	0.2467%
47	0.5226	0.4852	3.6314	3.6316	7.16203%	0.0055%
187	0.7657	0.8578	4.3073	4.3092	12.0723%	0.0441%
197	0.6534	0.7863	4.7450	4.7375	20.4978%	0.1581%

Case (3) Three pressure taps non-Gaussian simulation of dome (*h:l*=1:5) (windward)

Point*	Skewness		Kurtosis		Sum of % diff. from target	% diff. from kurtosis target
	Target	Simulated	Target	Simulated		
22	0.7254	0.7465	4.6915	4.6901	2.9386%	0.0298%
32	0.6023	0.5246	3.8021	3.8071	13.0320%	0.1315%
42	0.6541	0.5070	3.7300	3.7351	22.6257%	0.1367%
27	0.5062	0.4290	3.6014	3.6054	15.3620%	0.1111%
37	0.5311	0.6711	3.8384	3.8363	26.4151%	0.0547%
47	0.5226	0.4851	3.6314	3.6315	7.1784%	0.0028%
177	0.5544	0.662	3.7062	3.6854	19.9696%	0.5612%
187	0.7657	0.8577	4.3073	4.3086	12.0453%	0.0302%
197	0.6534	0.7869	4.7450	4.7376	20.5875%	0.1560%

Case (4) Four pressure taps non-Gaussian simulation of dome (*h:l*=1:5) (windward)

Point*	Skewness		Kurtosis		Sum of % diff. from target	% diff. from kurtosis target
	Target	Simulated	Target	Simulated		
14	0.4210	0.5212	3.9482	3.9505	23.8587%	0.0583%
22	0.7254	0.7477	4.6915	4.6903	3.0997%	0.0256%
32	0.6623	0.5241	3.8021	3.8078	21.0166%	0.1499%
42	0.6541	0.5085	3.7300	3.7492	22.7743%	0.5147%

*Note: Proposed points are located in Fig. 8

the windward side of the domes but negatively skewed on the leeward side of the dome. The skewness and kurtosis coefficients in leeward side are larger than the windward sides. The values of target and simulated higher order moments coefficients in Table 2 are in close proximity, and they are correlated each other. The error percent from kurtosis target is favorable with the better agreement occurring between the percent difference of targets and simulated higher order moments (see Table 2).

From Table 2, the simulated kurtosis values are very close to their targets. It can be found to emphasize in terms of kurtosis only to get target values which now will become a single target for this simulation technique and it is important parameter to get a non-Gaussian signal. The error percents from kurtosis target in windward sides are in the range below 1%, but the one in leeward side is greater than 1%. From those reasons, the windward of domes is better than the leeward to match well with their targets by using this simulation technique.

Table 3 Resultant error in the ensemble-averaged skewness and kurtosis values of simulation

Number of taps & Types of dome	Proposed pressure taps	Ensemble-averaged skewness		Ensemble-averaged kurtosis		%Diff. from skewness target	%Diff. from kurtosis target	Sum of % diff. from target
		Target	Simulated	Target	Simulated			
Two pressure taps (h:l=1:2) windward	13-20 & 187- 201	0.4620	0.4920	3.8523	3.8592	6.4935%	0.1719%	6.6654%
Two pressure taps (h:l=1:2) leeward	85-99 & 128-140	-0.9682	-0.9673	8.0410	8.2599	0.0930%	2.7222%	2.8153%
Two pressure taps (h:l=1:5) windward	22-32, 32-42, 37-47 & 187-197	0.6364	0.6531	4.1065	4.1100	2.6200%	0.0850%	2.7050%
Three pressure taps (h:l=1:5) windward	22-32-42, 27-37-47 & 177-187-197	0.6128	0.6298	4.0059	4.0041	2.7700%	0.0450%	2.8150%

*Note: Proposed points are located in Fig. 8

Table 3 presents the errors for the windward and leeward sides of different rise-span ratios of domes using two pressure taps and the windward side of dome (h:l=1:5) for two, three and four pressure taps respectively. Ensemble averaged values are shown. The simulation results compare favorably with their corresponding targets. The discrepancies of kurtosis between the simulations and the targets are all less than 5%. The error in the simulation of skewness is slightly larger than kurtosis. However, the kurtosis is much more important for the description of intensity of pressure fluctuations. The better simulation of kurtosis in this manuscript can well reflect the non-Gaussian feature of pressure fluctuations. Smaller discrepancies occur the windward side of dome (h:l=1:5) than on both sides of dome (h:l=1:2).

4.2. Targets and simulations of wind pressure time series and PSDs

The wind pressure time histories present in the form of pressure coefficient (C_p) versus time (sec). From the left sides of Figs. 9-13, the non-Gaussian processes on windward side are slightly more similar than the leeward side to their targets because the pressure fluctuations in leeward sides has been occupied the higher moments than the one in windward side. The windward sides of domes appear positively going spikes which induce the low skewness and occupied the less kurtosis coefficients (see Table 2). Due to these reasons, the one in leeward side is hard to match easily with their targets by using this simulation technique.

The right sides of Figs. 9-13 present the target and simulated power spectral densities (PSDs) in the form of $PSD(m^2/s)$ versus frequency (Hz). They show that the accuracy of this simulation technique is heavily dependent on the PSDs in windward and leeward sides of domes. The comparison of observed

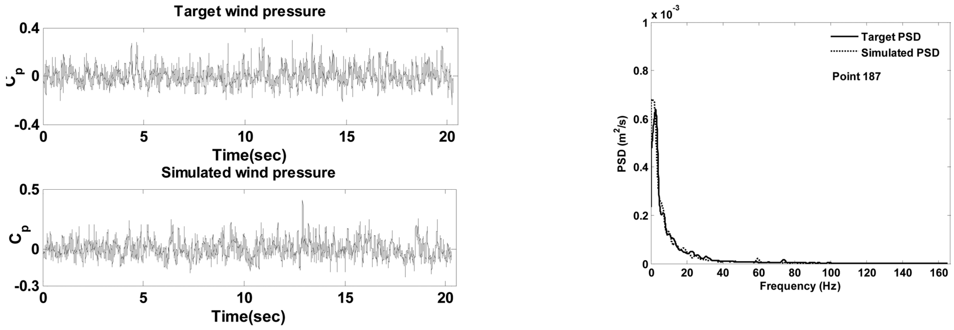

Left: fluctuating wind pressure data. Right: power spectral density (PSD)

Fig. 9 Comparison of target and simulation of pressure time series and PSD using two pressure taps on dome (*h:l*=1:2) (windward)

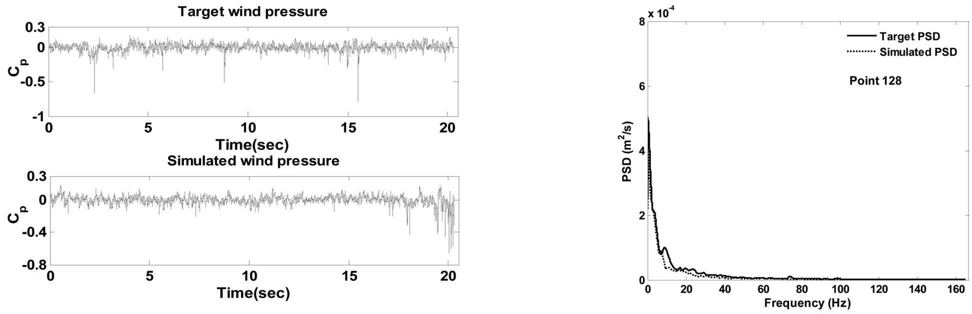

Left: fluctuating wind pressure data. Right: power spectral density (PSD)

Fig. 10 Comparison of target and simulation of pressure time series and PSD using two pressure taps on dome (*h:l*=1:2) (leeward)

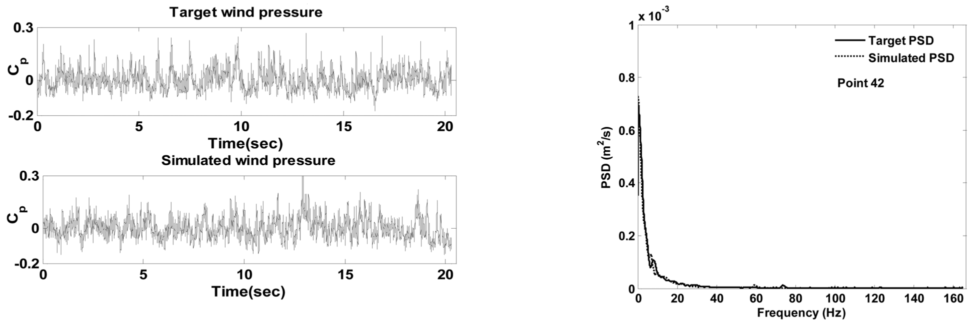

Left: fluctuating wind pressure data. Right: power spectral density (PSD)

Fig. 11 Comparison of target and simulation of pressure time series and PSD using two pressure taps on dome (*h:l*=1:5) (windward)

and simulated PSDs is favorable, with the better agreement occurring between the higher frequency range than the lower frequency range. Moreover, the PSDs in windward sides seem match well than the one in leeward side of dome to converge with their targets because the leeward side occupies the higher and negative skewness of signals and spectra normalized (see Fig. 14) of leeward is larger than the windward in higher frequency region (Zou *et al*. 2008).

The canonical equation of the wavelet transforms combined with ARMA model is based on the

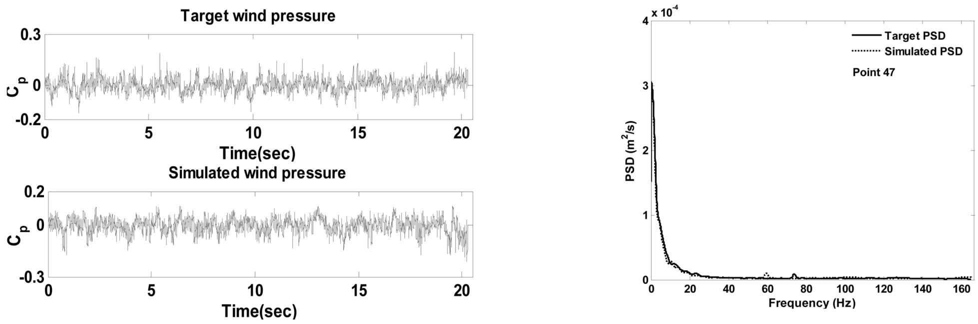

Left: fluctuating wind pressure data. Right: power spectral density (PSD)

Fig. 12 Comparison of target and simulation of pressure time series and PSD using three pressure taps on dome (*h:l*=1:5) (windward)

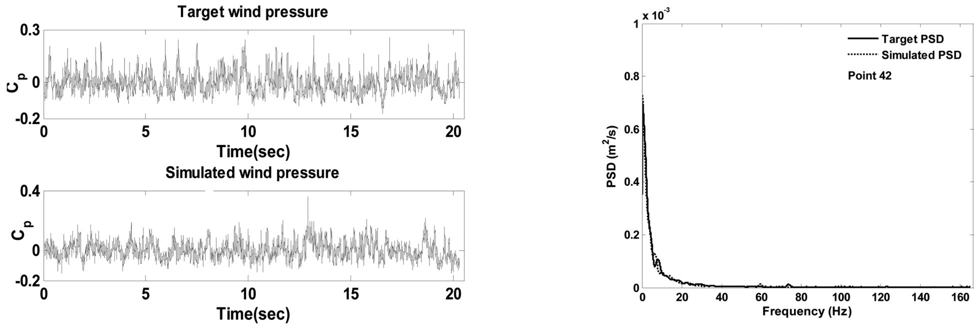

Left: fluctuating wind pressure data. Right: power spectral density (PSD)

Fig. 13 Comparison of target and simulation of pressure time series and PSD using four pressure taps on dome (*h:l*=1:5) (windward)

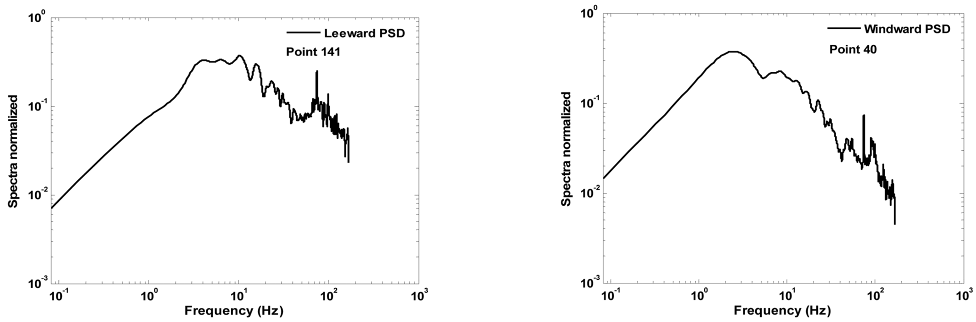

(a) (b)

Fig. 14 Power spectra of wind pressure components (a) leeward side and (b) windward side

minimum mean square of prediction error. The prediction error filters have decorrelation effect on the wavelet transform combined with ARMA process. The spectra of wind field have comparatively large variation by the frequency range. There is more content at low frequency, but less content at high frequency. The decorrelation effect makes spectra to be average. It leads to significant influence to the low frequency range, but has little influence to the high frequency range.

In the case of multivariate non-Gaussian simulation, these results are only considered on the windward and leeward sides of domes, but have no effects on the angle of direction of domes because the proposed pressure taps are presented in the same sides, being close each other and they occupied the same characteristics of spectra.

4.3 Targets and simulations of CPSDs for multivariate simulation

The targets and simulated cross-power spectral densities (CPSDs) also present in the form of CPSD (m^2/s) versus the frequency (Hz) (see Figs. 15, 16, 18 and 19). The cross-power spectral density (CPSD) is calculated from

$$S_{xy}(n) = \sqrt{\gamma_{xy}^2(n) S_{xx}(n) S_{yy}(n)} \tag{20}$$

where $S_{xy}(n)$ is the cross-power spectral density, $\gamma_{xy}^2(n)$ is the coherence squared function, $S_{xx}(n)$ is the weighted PSD of the lower pressure tap and $S_{yy}(n)$ is the weighted PSD of the higher pressure tap.

Figs. 15 and 16 show the comparison of target and simulated CPSDs on windward and leeward sides of domes. It can be found that the comparisons of CPSDs on windward sides are slightly better than the one of leeward side, but some pressure taps on windward sides are distorted from their targets on the range of low frequency.

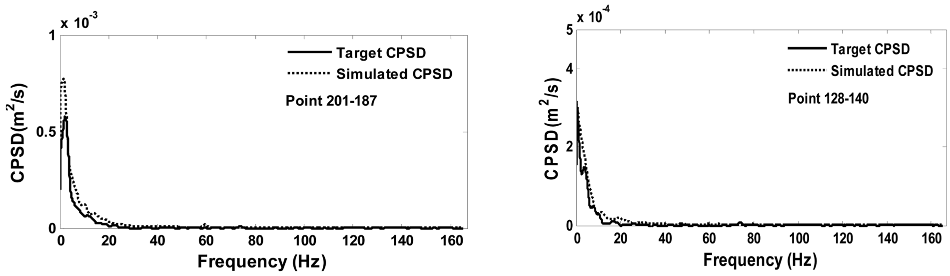

Left: windward side. Right: leeward side

Fig. 15 Comparison of target and simulation of CPSD using two pressure taps on dome (*h*:*l*=1:2) (windward and leeward)

on dome (*h*:*l*=1:2) (windward and leeward)

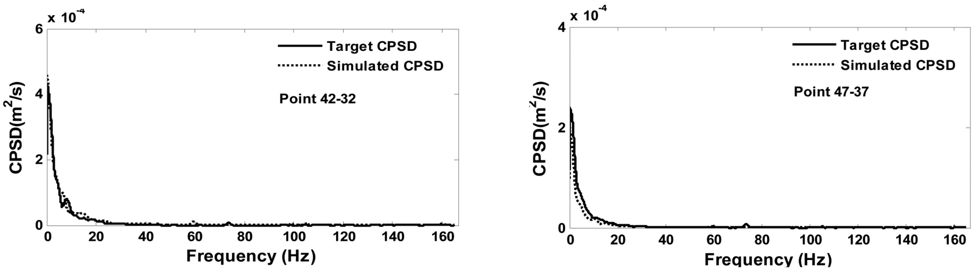

(a) (b)

Fig. 16 Comparison of target and simulation of CPSD using two pressure taps on dome (*h*:*l* = 1:5) (windward)

Fig. 17 shows the characteristics of CPSDs on the windward-windward and leeward-leeward of domes. The normalized cross-spectrum on the leeward side is larger than the one of windward in higher frequency. Comparing the peak cross-spectra of leeward and windward sides, the windward one shows the peak in low frequency range is larger than the higher frequency, but the one in leeward spectrum is almost similar to each other. Due to these reasons, the cross-spectra in leeward side also cause more distortion from their targets than the one in windward side.

Fig. 18 gives a good comparison of the target and simulated CPSDs, and it seems to match with their targets on both the range of low and high frequency. It is expected that the CPSDs will be in better agreement for two taps in close proximity than two taps spaced further apart. It can be found

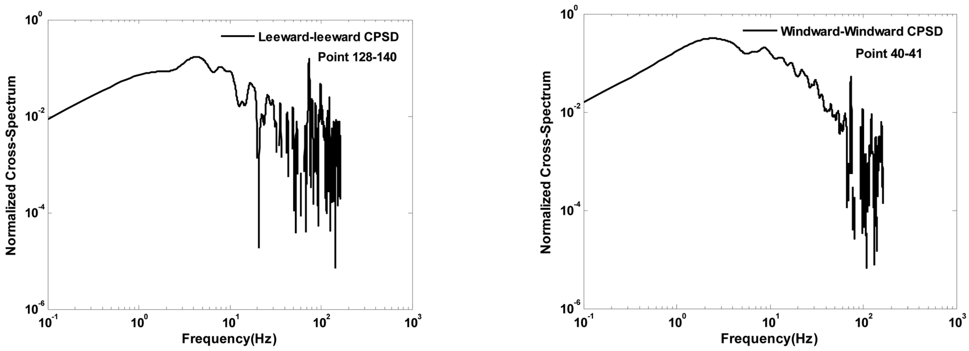

(a) (b)

Fig. 17 Cross-spectra of wind pressure components (a) leeward side and (b) windward side

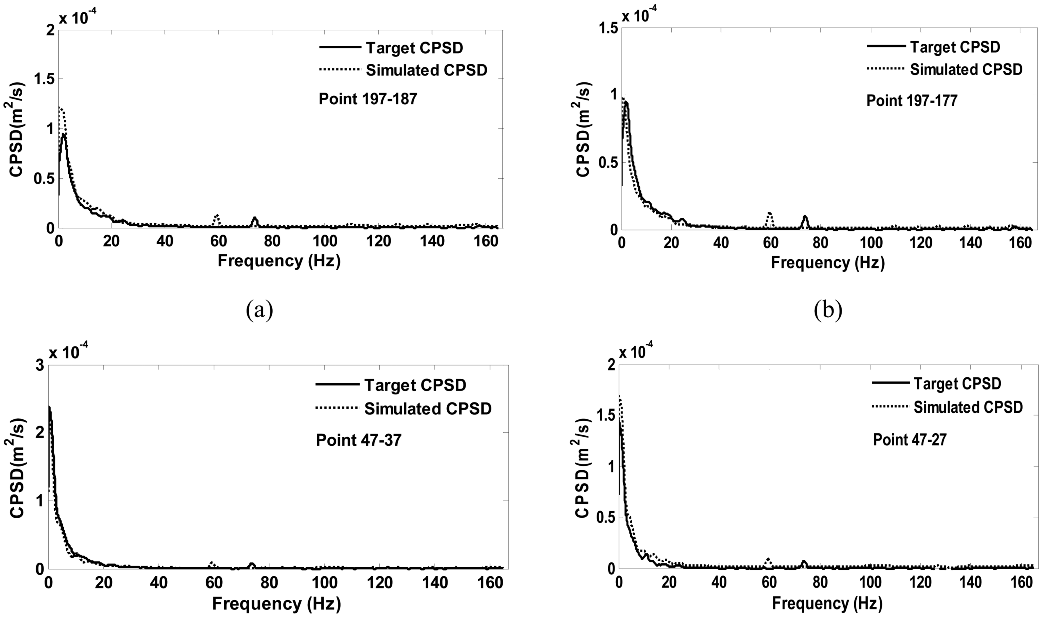

(a) (b) (c) (d)

Fig. 18 Comparison of target and simulation of CPSD using three pressure taps on dome (h:l=1:5) (windward) that the coherence model gives a smaller error at the two adjacent pressure taps, but it gives the larger error at the two non-adjacent pressure taps. Because, the residual errors (*residual= data-fit*) between the fitting curve and the experimental data of coherence function at the adjacent pressure taps are less than the one of coherence function at the non-adjacent pressure taps in the derivation of this coherence model using overall least-squares fit with the help of MATLAB. For these reasons, the simulated cross-power spectra of two adjacent pressure taps are more convergent with their targets, but those of the two non-adjacent pressure taps are more distorted from their targets. Fig. 19 also compares the target and simulated cross-spectral functions of the four pressure taps in the significant frequency range. The match between target and simulated cross-spectra are excellent in the low frequency range where there is significant energy, but the target and simulated CPSDs of the furthest two pressure taps in Fig. 19(c) give the worst comparison with this simulation technique.

Fig. 20 shows the comparison of ensemble-averaged simulations and the targets of CPSDs using two pressure taps on the windward side and leeward side of dome ($h{:}l = 1{:}2$). The ensemble averaging of co-spectra are considered by point pairs separated with same distance, such as points 13-20, 187-201 and 85-99 (see Fig. 8), etc. It can be found that both sides of co-spectra in Fig. 20 have small discrepancies between the ensemble-averaged co-spectra and their targets. Fig. 21 also shows the comparison using two pressure taps on the windward side of dome ($h{:}l = 1{:}5$),

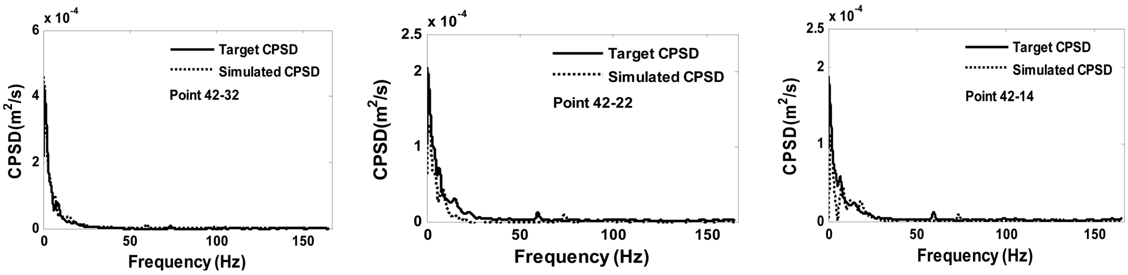

(a) (b) (c)

Fig. 19 Comparison of target and simulation of CPSD using four pressure taps on dome ($h{:}l$=1:5) (windward)

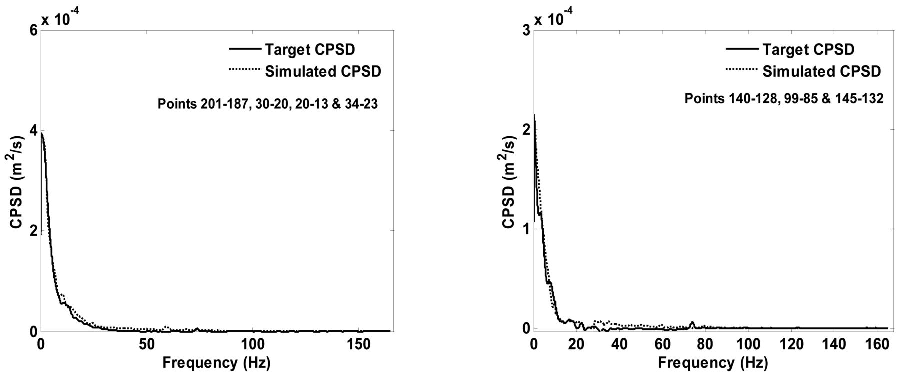

(a) Windward side **(b) Leeward side**

Fig. 20 Comparison of ensemble average simulation and target of CPSD using two pressure taps on domes ($h{:}l$=1:2)

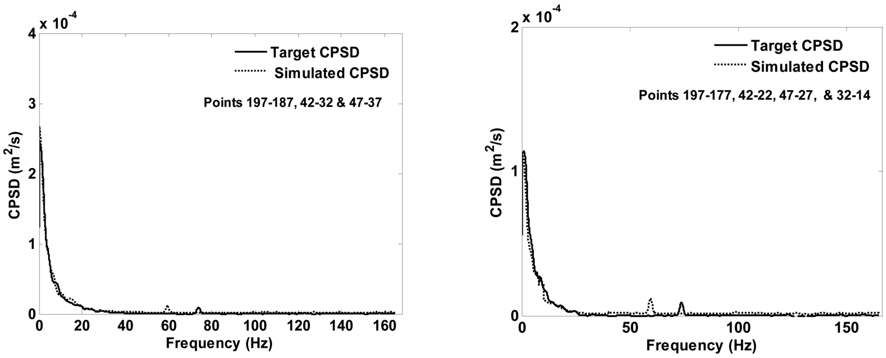

(a) Pairs of two adjacent points (b) Pairs of two non-adjacent points

Fig. 21 Comparison of ensemble average simulation and target of CPSD using two pressure taps on domes (h:l=1:5) (windward)

respectively. These figures demonstrate good agreement between the target and simulated cross-spectra. The small discrepancies of the values of co-spectra in dome (h:l=1:5) occur to compare with dome (h:l=1:2). Furthermore, due to the residual errors, it is found that the errors of the adjacent pressure taps is less than the non-adjacent pressure taps. Therefore, Fig. 21(a) is better agreement of the small discrepancies occurring between the comparisons of ensemble-averaged simulation and the target of co-spectra.

5. Discussion

There are five comparisons for multivariate non-Gaussian simulation in this research such as skewness and kurtosis coefficients, wind pressure time histories, PSDs and CPSDs. Among them, as the validation of multivariate non-Gaussian simulation using the wavelet-based CDF mapping technique, the comparisons of PSDs in all taps give the best results by using this simulation technique. The CPSDs also compare favorably. The simulated skweness and kurtosis coefficients approach to their targets. Nevertheless, the error percent between the target and simulated higher order moments coefficients and the similarity between the target and simulated signals in terms of PSDs and CPSDs in all pressure taps generally seem to be good.

6. Conclusions

This paper presents the simulation of multivariate non-Gaussian wind pressure on spherical latticed domes using a wavelet-based CDF mapping technique. This multivariate Gaussian simulation is transformed into multivariate non-Gaussian simulation by using CDF mapping technique (Masters and Gurley, 2003). The validations and limitations of multivariate non-Gaussian simulation of wind pressure on the separated flow regions of different rise-span ratio of domes using CDF mapping technique are as follows:

(1) All results of simulated skewness and kurtosis coefficients in multivariate non-Gaussian simulation are satisfied to match with their targets by using this simulation technique. But, the

percent errors from the target kurtosis is in the better agreement than the sum percent error and the percent error in windward sides are created better than the one in leeward side.
(2) Regarding wind pressure time histories, the one in windward side slightly seems similar with the targets more than the one in leeward side using this simulation technique.
(3) Comparison of observed and simulated power spectra is favorable, with the better agreement occurring between the higher frequency range and the lower frequency range. Furthermore, the spectra for the windward sides are created better than the leeward side.
(4) Due to the residual errors (*residual= data-fit*) between the fitting curve and the experimental data of coherence function at the adjacent pressure taps are less than the one of coherence function at the non-adjacent pressure taps, the simulated cross-power spectra of two adjacent pressure taps match well with their targets. The cross-spectra in leeward side are more distortion from their targets than the one in windward side because the windward sides occupy the lower and positive skewness of signals and the cross-spectra of the windward one shows the peak in low frequency range is larger than the higher frequency, but the one in leeward spectrum is almost similar to each other.
(5) Simulation of multiple, correlated wind pressure on different rise-span ratios of domes demonstrates satisfactory performance of the method. Multivariate non-Gaussian simulation of wind pressure of domes also produces a reasonable representation of the target moments, PSDs and CPSDs.

Acknowledgements

The authors gratefully acknowledge the financial support provided by National Natural Science Foundation of China (50678036). Additional support was provided from the Wind Engineering Research Laboratories Center of the Hunan University in China.

References

Bendat, J.S. and Piersol, A.G. (1986), *Random data: Analysis and measurement procedures*, 2nd Ed., New York, 86-125.

Borgman, L.E. (1990), *Irregular ocean waves: Kinematics and forces: the sea*, (Eds., LeMehaute, B. and Hanes, D.M.), John Wiley and Sons, 121-167.

Cai, G.Q. and Lin, Y.K. (1996), "Generation of non-Gaussian stationary stochastic processes", *J. Phys. Rev. E*, **91**, 737-765.

Daubechies, I. (1992), *Ten lectures on wavelets*, SIMA: Philadelpia, 17-48.

Deodatis, G. and Micaletti, R.C. (2002), "Simulation of highly skewed non-Gaussian stochastic processes", *J. Eng. Mech.- ASCE*, **127**(12), 1284-1295.

Elishakoff, I., Ren, Y.J. and Shinozuka, M. (1994), "Conditional simulation of non-Gaussian random-fields", *Eng. Struct*., **16**(7), 558-563.

Grigoriu, M. (1984), "Crossing of non-Gaussian translation processes", *J. Eng. Mech.- ASCE*, **110**(4), 610-620.

Grigoriu, M. (1993), "On the spectral representation method in simulation", *Probabilist. Eng. Mech*., **8**(2), 75-90.

Grigoriu, M. (1998), "Simulation of stationary non-Gaussian translation processes", *J. Eng. Mech.- ASCE*, **124**(2), 121-126.

Gurley, K.R. (1997), *Modeling and simulation of non-Gaussian processes*, PhD. Thesis, Notre Dame: University of Notre Dame. 2-15.

Gurley, K.R. and Kareem, A. (1997a), "Analysis, interpretation, modeling and simulation of unsteady wind and

pressure data", *J. Wind Eng. Ind. Aerod*., **69-71**, 657-669.
Gurley, K. and Kareem, A. (1997b), "Application of wavelet transforms in signal characterization", *Eng. Struct*., **3**, 855-875.
Gurley, K.R. and Kareem, A. (1998a), "A conditional simulation of non-normal velocity/pressure fields", *J. Wind Eng. Ind. Aerod.*, **77-78**, 39-51.
Gurley, K. and Kareem, A. (1998b), "Simulation of correlated non-Gaussian pressure fields", *J. Wind Eng. Ind. Aerod.*, **33**(3), 309-317.
Griguriu, M. (2007), "Parametric translation models for stationary non-Gaussian processes and fields", *J. Sound Vib*., **303**(3-5), 428-439.
Hoshiya, M., Noda, S. and Inada, H. (1998), "Estimation of conditional non-Gaussian translation stochastic fields", *J. Eng. Mech.- ASCE*, **124**(4), 435-445.
Huang, S.P., Phoon, K.K. and Quek, S.T. (2000), "Digital simulation of non-Gaussian stationary processes using
Karhunen-Loeve expansion", *Proceedings of the 8th ASCE Specialty Conference on Probabilistic Mechanics and Structural Reliability*, 1-6.
Kumar, K.S. (1997), *Simulation of fluctuation wind pressure on low building roofs*, Ph.D Thesis, Canada: Concordia University, 135-165.
Kumar, K.S. and Stathopoulos, T. (1998), "Power spectra of wind pressures on low building roofs", *J. Wind Eng. Ind. Aerod.*, **74**(76), 665-674.
Kumar, K.S. and Stathopoulos, T. (1999), "Synthesis of non-Gaussian wind pressure time series on low building roofs", *Eng. Struct.*, **21**(12), 1086-1100.
Kitagawa, T. and Nomura, T. (2003), "A wavelet-based method to generate artificial wind fluctuation data", *J. Wind Eng. Ind. Aerod.*, **91**(1), 943-964.
Li, Chao, Li, Q.S., Huang, S.H., Fu, J.Y. and Xiao, Y.Q. (2010), "Large eddy simulation of wind loads on a large-span spatial lattice roof ", *Wind Struct*., **13**(1), 57-82.
Li, Y.S. and Kareem, A. (1997), "Simulation of multivariate nonstationary random processes: Hybrid DFT and digital filtering approach", *J. Eng. Mech.- ASCE*, **123**(12), 1302-1310.
Master, F.J. and Gurley, K.R. (2003), "Non-Gaussian simulation: cumulative distribution function map-based spectral correction", *J. Eng. Mech.- ASCE*, **129**(12), 1418-1428.
Masters, F.J. (2004), *Measurement, modeling and simulation of ground-level tropical cyclone winds*, PhD. Thesis, Florida: University of Florida, 27-59.
Masters, F.J., Gurley, K. and Kopp, G.K. (2010), "Multivariate stoachastic simulation of wind pressure over lowrise structures through linear model interpolation", *J. Wind Eng. Ind. Aerod.*, **98**(4-5), 226-235.
Nyi, N.A. and Ye, J.H. (2010), "Coherence of wind pressure on domes", J. *Southeast University* (English Edition), **26**(1), 100-106.
Priestley, M.B. (1967), "Power spectral analysis of non-stationary processes", *J. Sound Vib*., **6**(1), 86-97.
Popescu, R., Deodatis, G. and Prevost, J.H. (1998), "Simulation of homogeneous on-Gaussian stochastic vector fields", *Probabilist. Eng. Mech*., **13**(1), 1-13.
Phoon, K.K., Haung, S.P. and Quek S.T. (2002), "Simulation of second-order processes using Karhunen-Loeve expansion", *Comput. Struct*., **80**(12), 1049-1060.
Shinozuka, M. and Jan, C.M. (1972), "Digital simulation of random processes and its applications", *J. Sound Vib*., **25**(1), 111-128.
Spinelli, P. (1987), "Artificial wind generation and structural response", *J. Struct. Eng.- ASCE*, **113**(12), 2382-2398.
Shinozuka, M. and Deodatis, G. (1991), "Simulation of stochastic processes by spectral representation", *J. ASEM Appl. Mech. Rev*., **44**(4), 191-203.
Shinozuka, M. and Deodatis, G. (1996), "Simulation of multi-dimensional Gaussian stoachastic fields by spectral representation", *J. ASEM Appl. Mech. Rev*., **49**(1), 29-53.
Seong, S.H. and Peterka, J.A. (1997), "Computer simulation of non-Gaussian multiple wind pressure time series", *J. Wind Eng. Ind. Aerod.*, **72**, 95-105.
Sakamoto, S. and Ghanem, R. (2002), "Simulation of multi-dimensional non-Gaussian non-stationary random fields", *Probabilist. Eng. Mech*., **17**(2), 167-176.
Steinwolf, A. (2006), "Random vibration testing beyond PSD limitations", *J. Sound Vib*., **32**, 12-21.

Steinwolf, A. and Stepten, A.R. (2006), "Non-Gaussian alaysis of turbulent boundary layer fluctuating pressure on aircraft skin panels", *J. Aircraft*, **42**(6), 1662-1675.

Su, Y. (2007), *Characteristics of wind loading on long-span roofs in chinese*, Ph.D Thesis, Harbin, Harbin Institute of Technology.

Vanmarcke, E.H. and Fenton, G.A. (1991), "Conditioned simulation of local fields of earthquake ground motion", *Struct. Saf.*, **10**(1-3), 247-264.

Yamazaki, F. and Shinozuka, M. (1998), "Digital generation of non-Gaussian stochastic fields", *J. Eng. Mech - ASCE.*, **114**(7), 1183-1197.

Zeldin, B.A. and Spanos, P.D. (1996), "Random field representation and synthesis using wavelet bases", *J. Appl. Mech.-T ASME*, **63**(12), 946-952.

Zhang, R.C. and Deodatis, G. (1996), "Seismic ground motion synthetics of the 1989 Loma Prieta earthquake", *Earthq. Eng. Struct. D.*, **25**(5), 465-481.

Zou, Lianghao, Liang, Shuguo, Li, Q.S. and Zhao, Lin and Ge, Yaojun (2008), "Investigation of 3-D dynamic wind loads on lattice towers", *Wind Struct.*, **11**(4), 323-340.

CC